High-pressure compression behavior of isoelectronic pairs of alkali metal halides and noble gas solids

Jialin Lei, Minseob Kim, Jinhyuk Lim,* and Choong-Shik Yoo†
Institute of Shock Physics and Department of Chemistry, Washington State University, Pullman, Washington 99164, USA

(Received 25 March 2021; revised 13 June 2021; accepted 2 August 2021; published 13 August 2021)

We have studied the compression behaviors of Ne, Ar, and Kr in comparison with the isoelectronic counterparts of NaF, KCl, and RbBr to 120 GPa, using *in situ* angle-resolved x-ray diffraction. Interestingly, the pressure-volume compression data indicate the emergence between the isoelectronic pairs of NaF/Ne >60 GPa, KCl/Ar >30 GPa, and RbBr/Kr >25 GPa—analogous to that previously observed in CsI/Xe >80 GPa. The interatomic distances of the isoelectronic pairs also become similar as pressure increases, within the difference of ∼3%, underscoring the pressure-induced electron polarization in novel gas solids, stronger in Xe and getting weaker in Kr, Ar, and Ne. In contrast, the compression curves and interatomic distances of He and LiF remain distinctive to 200 GPa.

DOI: 10.1103/PhysRevB.104.064107

I. INTRODUCTION

The nature of chemical bonding in dense solids at extreme conditions can be quite different from what we know at low pressures, especially in the regime where strong coulombic interactions become dominant over electron hybridization [1–3]. A perfect display of this conjecture is the nearly identical density between inert gas solid Xe and ionic solid CsI > ∼ 80 GPa [4,5], while exhibiting completely different density and chemical bonding at ambient condition. Xe transforms from face-centered cubic (fcc) to hexagonal close-packed (hcp) structure martensitically over a wide pressure range between 3 and 70 GPa [6,7], while CsI transforms to an orthorhombic *Pnma* structure with a hcp stacking which resembles hcp Xe at ∼50 GPa [4,5]. The high-pressure orthorhombic phase of CsI becomes metallic >115 GPa and even superconducting >180 GPa at a critical temperature of ∼2 K [8]. Interestingly, Xe also becomes metallic at 132 GPa [9], but the superconductivity has not been observed at higher pressure.

Xe is isoelectronic to CsI. Interestingly, theory predicts that the superconductivity in CsI is originated from a peculiar reverse electron transfer from 5*p* I to 6*s* Cs [10], resulting in the same chemical bonding and close electronic-shell configuration between CsI and solid Xe. This, however, seems counterintuitive to the conventional chemical notion, as iodine is more electronegative and cesium is more electropositive. An alternative explanation may be that, under high pressure, the electron cloud of large Xe becomes more polarized through an electron transfer between adjacent Xe atoms, giving rise to partially charged $Xe^{\delta+}$ and $Xe^{\delta-}$ and becoming more ionic bonding as in $Cs^{+}I^{-}$. This conjecture stems from the electrostatic coulombic stabilization and densification at high pressures [1].

One reasonable deduction from the high-pressure compression behavior of isoelectronic Xe and CsI is whether other inert gas solids such as Ne, Ar, and Kr can be polarized under high pressures and, if they can, to what extend with respect to their isoelectronic counterparts of alkali metal halides, NaF, KCl, and RbBr. This has not been explored but is important to understand the evolution of chemical bonding in these isoelectronic pairs and in other molecular solids [1]. Therefore, we have studied high-pressure compression behaviors of NaF/Ne, KCl/Ar, and RbBr/Kr using angle-dispersed x-ray diffraction (ADXD) and determined their equations of state (EOSs) and crystal structures. The results show the emerging pressure-volume (PV) compression curves between these isoelectronic pairs analogous to those in CsI/Xe, but distinctive to He/LiH.

II. EXPERIMENTAL METHODS

All high-pressure diffraction experiments were performed in a regular axial geometry using diamond anvil cells (DACs) with two opposing diamond anvils (Type Ia, 100 μm in diameter beveled at 8° from 300 μm flat). Rhenium gaskets were pre-indented to ∼30 μm in thickness, and we drilled small holes of ∼80 μm in diameter at the center using an electric discharge machine. Polycrystalline samples of NaF (99.99%, Sigma-Aldrich, USA), KCl (99.99%, Sigma-Aldrich, USA), and RbBr (99.6%, Sigma-Aldrich, USA) were used after heating at 450 K in vacuum oven for 1 h to remove any moisture contained. The dried samples were then loaded into DACs, together with a small piece of Cu chip as pressure calibrant [11], followed by loading high-pressure inert gas at 0.2 GPa using a custom-made high-pressure gas loader at Washington State University.

The ADXD experiments were carried out at third-generation synchrotron x-ray beamlines both 16-IDB and 16-BMD of High Pressure Collaborating Access Team

*Present address: University of Florida, Gainesville, FL 32611.
†Corresponding author: csyoo@wsu.edu

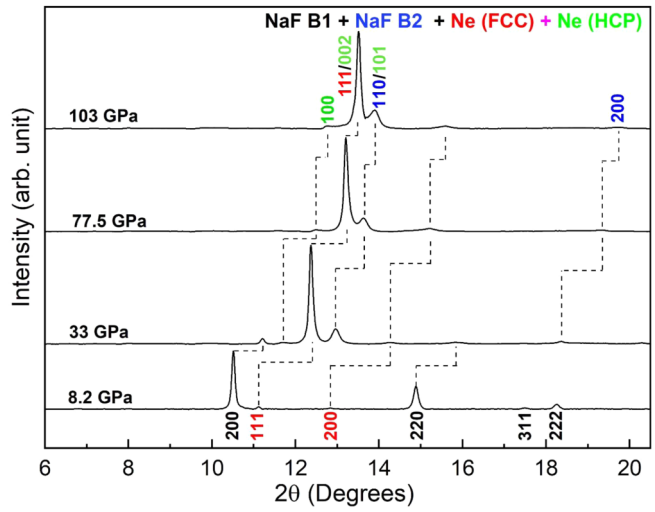

FIG. 1. A selected set of angle-resolved x-ray diffraction patterns of NaF/Ne at high pressures. The diffraction lines for B1 and B2 phases of NaF were indexed in black and blue; those for fcc and hcp phases of Ne were in red and green. The dashed lines are the guides for eyes.

(HPCAT) at the Advanced Photon Source (APS). For these ADXD experiments, we used microfocused (4×4 μm in beam size) monochromatic x ray (0.4066 Å at 16-IDB and 0.4133 Å at 16-BMD) and two-dimensional (2D) MAR image plate x-ray detectors. The diffraction geometry, such as the sample-to-detector distance, beam center, and detector tilt, was calibrated using a CeO_2 reference sample. The recorded 2D diffraction images were integrated with DIOPTAS [12] and then analyzed using XRDA [13].

III. RESULTS AND DISCUSSION

The diffraction experiments were performed for NaF/Ne to 120 GPa, KCl/Ar to 116 GPa, and RbBr/Kr to 46 GPa. Many diffraction images were acquired with a typical pressure increment of ~4 GPa. The resulting PV compression data are summarized in Table SI in the Supplemental Material [14].

Figure 1 shows the ADXD patterns of NaF/Ne at several pressures, highlighting the pressure-induced structure evolution. The B1 phase of NaF can be cleanly indexed to 33 GPa, above which its diffraction intensity drops significantly, and several new peaks emerge with growing intensity with pressure. The new peaks at $2\theta = 13°$ and 18.3° can be well indexed to (110) and (200), respectively, for the B2 phase of NaF, indicating the B1-B2 phase transition in NaF as previously observed [15,16]. Interestingly, the peak at $2\theta = 11.7°$ can be assigned to the (100) of hcp Ne. The most dominant (101) peak of hcp Ne is, however, overlapped with the (110) peak of the NaF B2 phase.

Hcp-Ne was determined with the (100), (101), and (102) peaks (see Fig. S1 in the Supplemental Material [14]). The (200) of hcp-Ne at $2\theta =\sim 11.5°$ overlaps with the (111) of fcc-Ne, thus, they are indistinguishable. Diffused hcp-Ne (101) and hcp-Ne (102) are shown in the 2D diffraction images. However, the peaks did not appear clearly in the integrated pattern because of relatively weak intensities with respect to the background. The calculated *c*/*a* ratio of hcp-Ne at 103 GPa is 1.622, which is close to the ideal value of the hcp structure. The stacking faults are evidenced by the diffuse spots shown in the inset.

The hcp phases for He [17], Ar [18,19], Kr [20,21], and Xe [22–24] have well been studied and characterized previously, but the experimental data for hcp Ne is lacking. As can be seen in Fig. 1, the fcc phase of Ne is still present up to the highest pressure achieved in our experiment, indicating that the fcc-hcp transition is not complete. The coexistence of fcc and hcp phases over a large pressure range is likely due to the small energy difference between the two phases <230 GPa [25,26]. Note that the observed peak intensity ratios are not matched to those of simulated patterns; for example, in the NaF-B2 phase, the (200) peak should be bigger than the (110) peak.

TABLE I. Birch-Murnaghan equation of state of alkali metal halides and inert gas solids in comparison.

Phases	K_0 (GPa), this paper	K_0 (GPa), in literature	V_0 (Å^3)	References
LiH B1	–	33.1	67.93	[27]
He hcp	–	0.225	45.57	[17]
NaF B1	51 ± 4 ($K' = 4.2 \pm 0.6$)	46.4	98.61	[15]
NaF B2	114.5 ± 3 ($K' = 4.0 \pm 2.9$)	103	19.99	[15]
Ne fcc	1.1 ± 0.3 ($K' = 10.4 \pm 2.3$)	1.0–1.43	88.97	[29–31]
Ne hcp	1.3 ± 0.6 ($K' = 9.2 \pm 3.2$)	1.9	44.48	[32]
KCl B1	–	16.8–17.4	62.36	[33–35]
KCl B2	19.0 ± 0.8 ($K' = 5.6 \pm 0.2$)	17.2–23.7	53.53	[33,34]
Ar fcc	1.4 ± 0.2 ($K' = 9 \pm 0.9$)	1.2–6.5	149.83	[19,36,41]
Ar hcp	1.9 ± 0.5 ($K' = 8.9 \pm 1.7$)	1.2–3.6	75.24	[18,19,42,43]
RbBr B1	–	15.9	317.21	[44,45]
RbBr B2	27.4 ± 1.8 ($K' = 4.1 \pm 0.3$)	18.4–22.2	65.4	[46,47]
Kr fcc	1.6 ± 0.3 ($K' = 9.4 \pm 1.5$)	1.4–4.3	197.28	[21,48,49]
Kr hcp	3.9 ± 0.5 ($K' = 6.9 \pm 0.6$)	2.7–4	88.7	[20,21,48]
CsI B2	–	18	47.66	[4,5]
CsI (*Cmcm*)	–	15.9	317.21	[10]
Xe fcc	–	4.3	252.21	[6]
Xe hcp	–	4.9	126.1	[6]

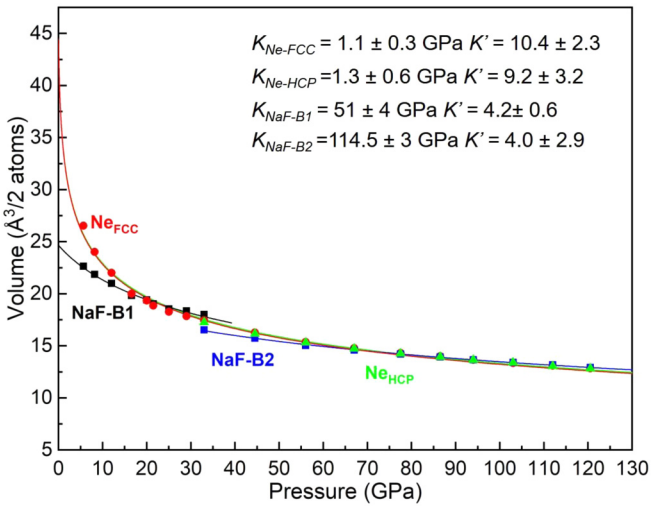

FIG. 2. Pressure-volume compression curves of NaF B1 (black), B2 (blue), Ne fcc (red), and hcp (green). The solid line is the best fit to the third-order Birch-Murnaghan equation of state. Error bars smaller than symbol size are omitted.

This can be understood in terms of the preferred orientation of multigrain of the heterogeneous sample.

The PV compression data of NaF and Ne are fitted to the third-order Birch-Murnaghan EOS (BM-EOS) [27] and plotted in Fig. 2. The resulting bulk modulus K_0, pressure derivative K', and the ambient unit cell volume values are summarized in Table I, in comparison with those obtained previously [28–49]. To compare with diatomic NaF, the volumes of two Ne atoms are plotted in Fig. 2. The compression curve for NaF shows a discontinuous volume change at ∼33 GPa, signifying the B1-to-B2 transition that occurs with a volume drop of 8.2%. This is consistent with the previous study [15]. In contrast, the hcp Ne shows nearly an identical compression curve as the fcc phase with no discontinuity in volume. As can be seen in the figure, the BM-EOS fits for Ne and NaF differ significantly <60 GPa. This is conceivable since the former is an inert gas solid formed through weak Van der Waals interactions, whereas the latter is ionic solid, where the cations and anions are bonded by strong coulombic forces. Interestingly, the EOS fits of hcp-Ne and B2-NaF gradually converge together and become almost undistinguishable >60 GPa.

The ADXD patterns for KCl/Ar and RbBr/Kr are shown in Fig. 3. The B1-B2 transition is not observed in our experiments, which start the compression at ∼7 GPa. The B1-B2 transitions occur at ∼2 GPa in KCl and 0.5 GPa in RbBr [35,47]. The observed diffraction peaks in Fig. 3 can be indexed well for the B2 phase of KCl to 116 GPa (a) and that of RbBr up to 46 GPa (b). Note that the diffraction peaks of KCl and RbBr remain relatively sharp to the highest pressure measured, whereas those of Ar and Kr become rapidly broadening as pressure increases. This is likely due to the stacking disorder developed in the fcc lattice with pressure and the fcc-to-hcp transition [6,7]. The hcp phase of Ar appears at ∼20 GPa as evident from the characteristic (100) peak at 2θ = 9.2°. More peaks become observable as increasing pressures. At 52 GPa, the (002) of hcp Ar separates out from the (110) of KCl and becomes distinguishable up to 116 GPa; so do the

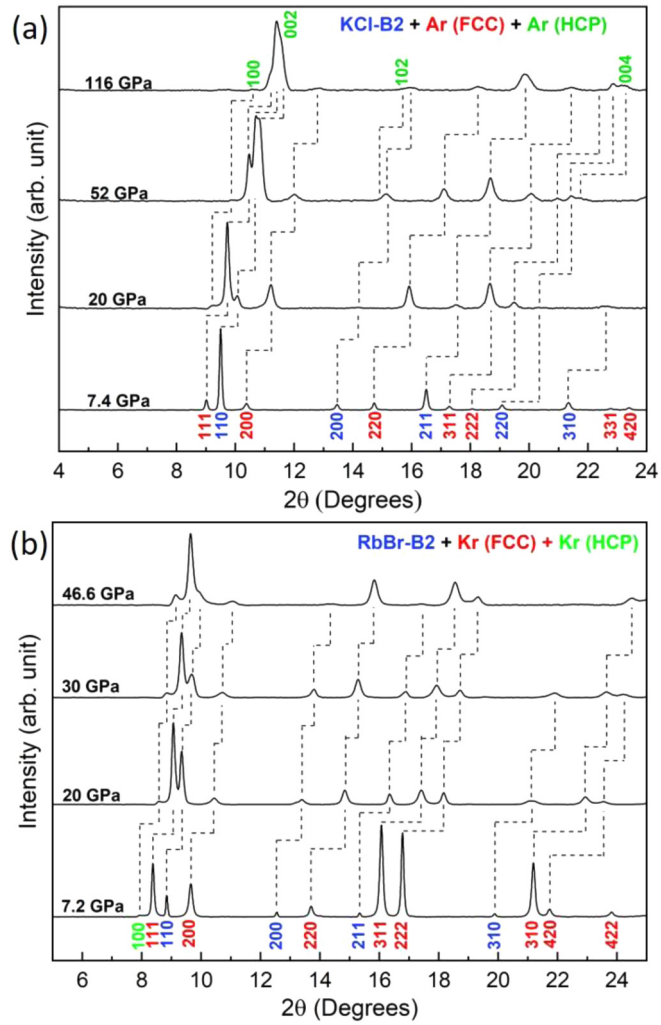

FIG. 3. X-ray diffraction patterns for (a) KCl/Ar and (b) RbBr/Kr. The (002) and (101) for the hcp phase of inert gas solids are found to be overlapped with the (111) of the fcc phase and (110) of the B2 phase for alkaline metal halides.

(102) and (004) peaks. The (100) peak of hcp Kr is observed at the pressure as low as ∼7 GPa with growing intensity with increasing pressure. This is consistent with the fcc-hcp transition pressure of Kr at ∼6 GPa previously reported [21]. Since the three phases are cubic or hcp with similar lattice parameters, the principal diffraction peaks appear at similar 2θ angles or overlap. Hcp-Kr was determined by the (100) and (101) peaks (see Fig. S2 in the Supplemental Material [14]). The diffused hcp-Kr (101) peak at 2θ =∼ 10.3° is covered again by the tail of strong fcc-Kr (111) and (200) peaks. The calculated c/a ratio of hcp-Kr at 46.6 GPa is 1.641, which is close to the ideal value of hcp.

The PV compression curves for KCl/Ar and RbBr/Kr are plotted in Fig. 4, together with those of LiH/He and CsI/Xe for comparison. The bulk moduli for fcc- and hcp-Ar phases are determined as 1.4 (±0.2) GPa and 1.9 (±0.5) GPa, consistent with the previously reported experimental and theoretical values in the range of 1.2–6.5 GPa for fcc-Ar [19,36–41] and 1.2–3.6 GPa for hcp-Ar [18,19,42,43]. It is interesting to note that the fcc-hcp phase transition in Ar accompanies

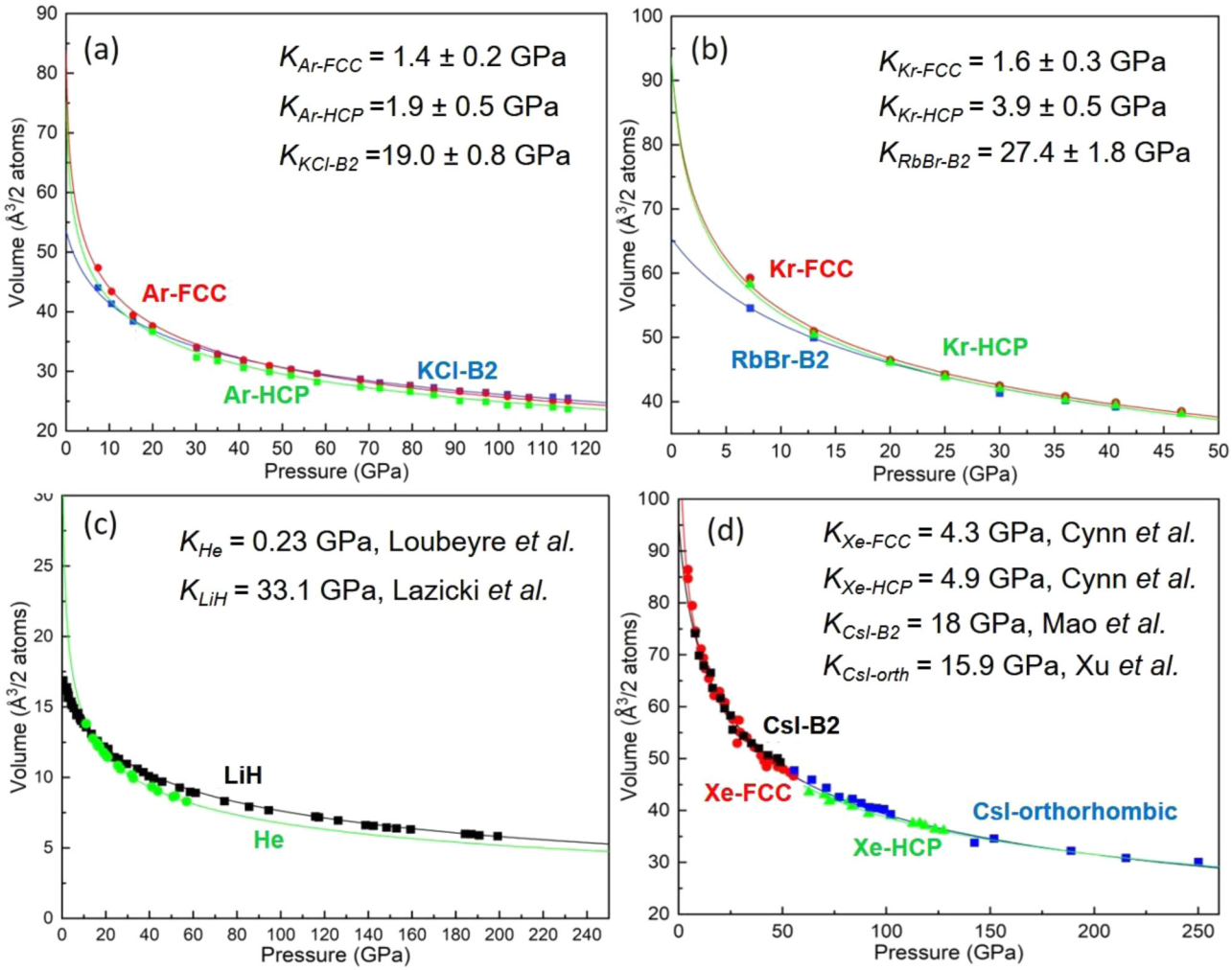

FIG. 4. Equation of state curves for (a) KCl/Ar, (b) RbBr/Kr, (c) LiH/He, and (d) CsI/Xe. The data plotted in (c) and (d) are from Refs. [16,27] and Refs. [5,6,10], respectively. All alkaline metals halides and inert gas solids show convergency in volume with increasing pressure, except helium and LiH.

a small volume drop of ∼2%, which is absent in Xe and Kr. Xe and Kr exhibit almost identical compression curves across the fcc-hcp transitions. The BM-EOS fits result in the bulk modulus values systematically increasing from Ne (1.3 GPa) to Ar (1.4 for fcc and 1.9 for hcp) to Kr (3.9 GPa). These values are also in good agreement with the literature values reported [20,21,48,49].

Like Ne/NaF and Xe/CsI, the compression curves of both Ar/KCl and Kr/RbBr converge >25–30 GPa. However, there is a discernable difference in the converging pressure; for example, the compression curve of Ne converges to that of NaF >60 GPa and Xe only >9 GPa. We attribute this difference to the apparent difference in polarizability in various inert gas solids. Clearly, Xe is the most polarizable followed by Kr, Ar, and Ne. In fact, the observed trend is also consistent with the fact that nearly nonpolarizable He clearly shows a different compression behavior from LiH to at least 200 GPa.

Figure 5 shows the interatomic distance of CsI and Xe as a function of pressure. Interatomic distances were obtained directly from the calculated volume because all atomic positions of B1 and B2 phases are fixed at the special

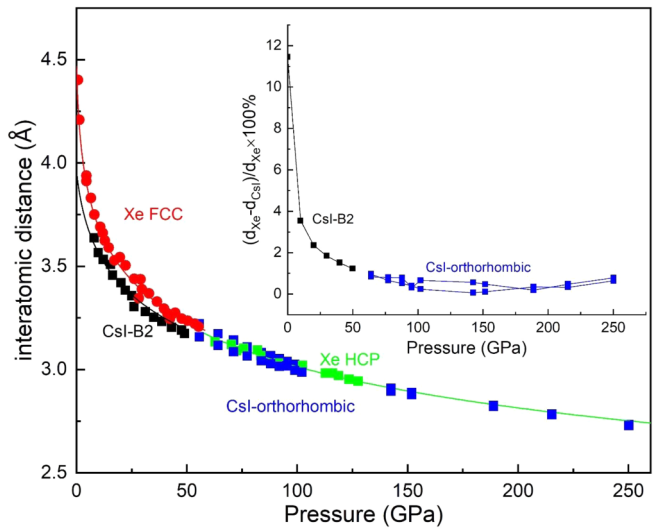

FIG. 5. Interatomic distance of CsI [4,10] and Xe [6] under pressures. Relative difference in interatomic distance between CsI and Xe are shown in inset.

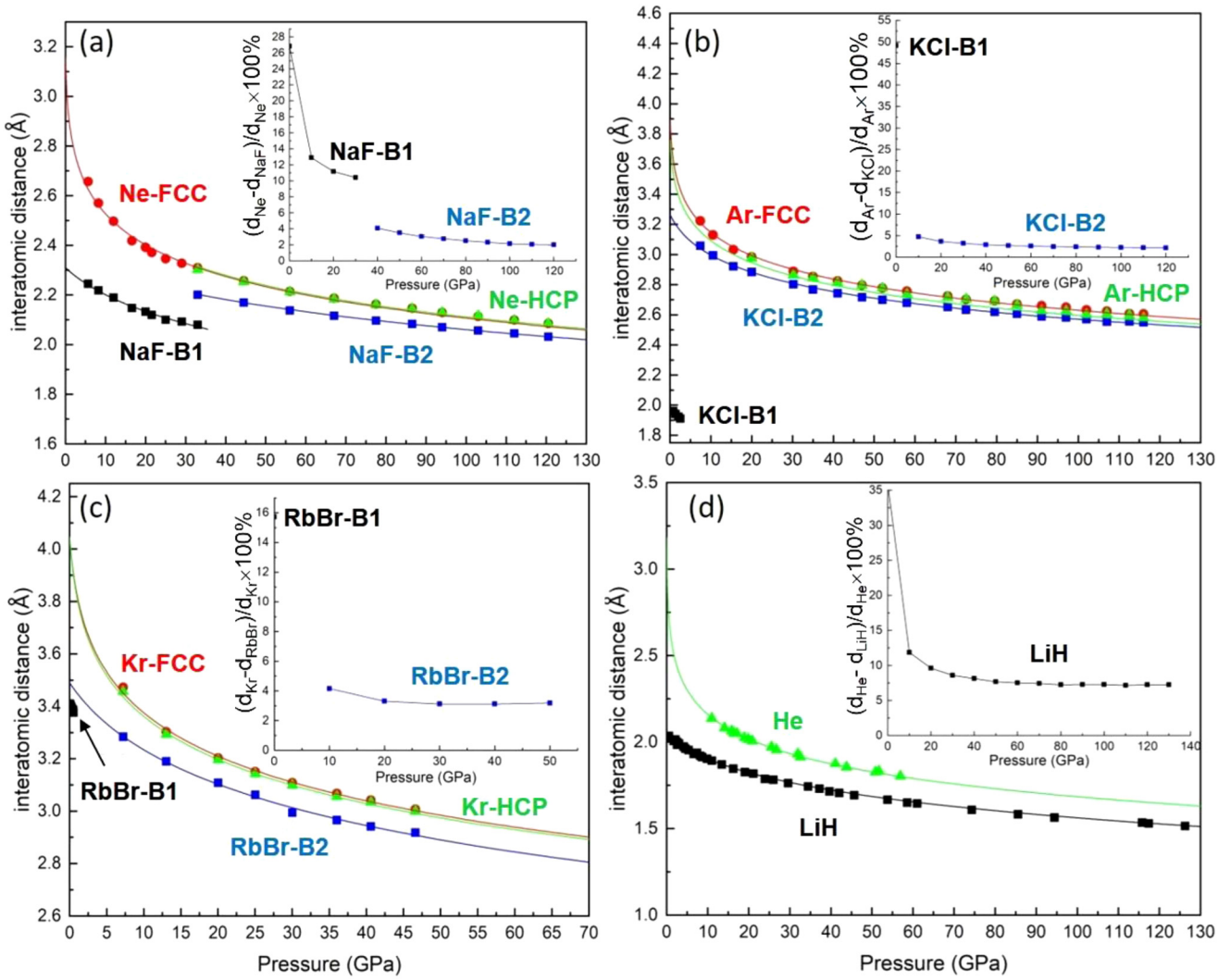

FIG. 6. Pressure dependence of interatomic distance for (a) NaF/Ne, (b) KCl/Ar, (c) RbBr/Kr, and (d) LiH [27]/He [16] showing small difference (2–3%) for Ne, Ar, and Kr and big difference (∼ 7.5%) for He.

position and assumed that the atoms stay in the same positions; 4*a*(0,0,0), 4*b*(1/2,1/2,1/2) sites of B1 phase and 1*a*(0,0,0), 1*b*($\frac{1}{2}$, $\frac{1}{2}$, $\frac{1}{2}$) sites of B2 phase, respectively. Therefore, the nearest neighboring atomic distance of B1 and B2 phases is directly calculated as $a\frac{\sqrt{3}}{2}$ where a is a unit cell parameter. In the same way, the nearest neighboring atomic distance of the fcc phase is $a\frac{\sqrt{2}}{2}$ with the atomic site at 4*a*(0,0,0). In hcp phase, atoms assigned at the 2*c* site, ($\frac{1}{3}$, $\frac{2}{3}$, $\frac{1}{4}$) and ($\frac{2}{3}$, $\frac{1}{3}$, $\frac{3}{4}$), and each cell parameter are refined.

Despite the specific volumes of CsI and Xe become nearly identical >9 GPa, there is a noticeable difference in bond distance between Cs-I and Xe-Xe up to 50–60 GPa. This may reflect a different nature of chemical bonding between CsI, where ionic bonds are dominant, and Xe, where the atoms are held together with van der Waals interactions. The B2 phase of CsI undergoes a phase transition to an orthodromic phase >50 GPa featuring two types of Cs-I bonds with different bond distances [10]. As shown in the figure, the two Cs-I bonds gradually merge and eventually become indistinguishable >100 GPa. On the other hand, the interatomic distance of Xe-Xe becomes very close to that of Cs-I >100 GPa within a difference <1%, as shown in the inset. This suggests that Xe-Xe bonds become more like Cs-I bonds.

Figure 6 plots the pressure dependence of interatomic distance in (a) NaF/Ne, (b) KCl/Ar, (c) RbBr/Kr, and (d) LiH/He. All but LiH show a similar trend. The interatomic distances of B2 phases are substantially smaller than those of B1 phases with the plateau values of 2–3% (see the insets), which is still greater than that for CsI/Xe (< 1%). It seems to suggest that the bonding in Ne, Ar, and Kr develop some ionic character at high pressure, as found in Xe but to a substantially smaller extent. He/LiH, however, shows a much greater difference in bond distance with a plateau value of ∼7.5%, indicating that the nature of chemical bonding in He up to 130 GPa remains unchanged.

IV. CONCLUSIONS

We have presented the PV compression data of three isoelectronic pairs of NaF/Ne, KCl/Ar, and RbBr/Kr up to ∼120 GPa, in comparison with those of He/LiH and Xe/CsI previously measured. The fcc-hcp phase transitions are

observed in all (but He) noble gas solids studied with notable differences at the transition pressures. The coexistence of the two phases is found over a wide range of pressures. The bulk moduli for alkali metal halides and inert gas solids are presented together with the PV compression curves that exhibit interesting convergent behaviors with increasing pressures. The interatomic distance in alkali metal halides were compared with that in inert gas solids, showing little difference ($< 1\%$) for Xe, small difference (2–3%) for Ne, Ar, and Kr, and big difference ($\sim 7.5\%$) for He. We attribute the pressure-induced convergence in the compression curves and interatomic distances to the pressure-induced polarization in noble gas solids under pressure, which appears the strongest in Xe, getting weaker in Kr, Ar, and Ne, and nearly absent in He.

ACKNOWLEDGMENTS

The x-ray diffraction experiments have been performed at the 16-IDB and 16-BMD beamlines of HPCAT/APS. We acknowledge Dr. Yue Meng and Dr. Changyong Park for their assistance at the beamline. This paper has been performed in support of the National Science Foundation (Grants No. DMR 1701360 and No. 2112653), US Department of Energy (DOE) National Nuclear Security Administration (NNSA; DE-NA0003918) and Army Research Office (Grant No. W911NF-17-1-0468). The operation of HPCAT/APS is supported by the DOE-NNSA's Office of Experimental Sciences. The APS is a DOE Office of Science User Facility operated for the DOE Office of Science by Argonne National Laboratory under Contract No. DE-AC02-06CH11357.

[1] C. S. Yoo, Matter Radiat. Extremes **5**, 018202 (2020).
[2] R. Jeanloz, Annu. Rev. Phys. Chem. **40**, 237 (1989).
[3] R. J. Hemley and N. W. Ashcroft, Phys. Today **51**(8), 26 (1998).
[4] H. K. Mao, Y. Wu, R. J. Hemley, L. C. Chen, J. F. Shu, L. W. Finger, and D. E. Cox, Phys. Rev. Lett. **64**, 1749 (1990).
[5] H. K. Mao, R. J. Hemley, L. C. Chen, J. F. Shu, L. W. Finger, and Y. Wu, Science **246**, 649 (1989).
[6] H. Cynn, C. S. Yoo, B. Baer,V. Iota-Herbei, A. K. McMahan, M. Nicol, and S. Carlson, Phys. Rev. Lett. **86**, 4552 (2001).
[7] E. Kim, M. Nicol, H. Cynn, and C. S. Yoo, Phys. Rev. Lett. **96**, 035504 (2006).
[8] M. I. Eremets, K. Shimizu, T. C. Kobayashi, and K. Amaya, Science **281**, 1333 (1998).
[9] K. A. Goettel, J. H. Eggert, I. F. Silvera, and W. C. Moss, Phys. Rev. Lett. **62**, 665 (1989).
[10] Y. Xu, J. S. Tse, A. R. Oganov, T. Cui, H. Wang, Y. Ma, and G. Zou, Phys. Rev. B **79**, 144110 (2009).
[11] A. Dewaele, P. Loubeyre, and M. Mezouar, Phys. Rev. B **70**, 094112 (2004).
[12] C. Prescher and V. B. Prakapenka, High Press. Res. **35**, 223 (2015).
[13] S. Desgreniers and K. Lagarec, J. Appl. Cryst. **31**, 109 (1998).
[14] See Supplemental Material at http://link.aps.org/supplemental/10.1103/PhysRevB.104.064107 for the PV compression data of inert gas solids and alkali metal halides (Table S1) and the refined diffraction patterns for NaF/Ne at 103 GPa (Fig. S1) and RbBr/Kr at 46 GPa (Fig. S2).
[15] Y. Sato-Sorensen, J. Geophys. Res. Solid Earth **88**, 3543 (1983).
[16] R. J. Hemley and R. G. Gordon, J. Geophys. Res. **90**, 7803 (1985).
[17] P. Loubeyre, R. LeToullec, J. P. Pinceaux, H. K. Mao, J. Hu, and R. J. Hemley, Phys. Rev. Lett. **71**, 2272 (1993).
[18] B. Li, G. Qian, A. R. Oganov, S. E. Boulfelfel, and R. Faller, J. Chem. Phys. **146**, 214502 (2017).
[19] D. Errandonea, R. Boehler, S. Japel, M. Mezouar, and L. R. Benedetti, Phys. Rev. B **73**, 092106 (2006).
[20] D. Errandonea, B. Schwager, and R. Boehler, High Press. Res. **22**, 375 (2002).
[21] D. Errandonea, B. Schwager, R. Boehler, and M. Ross, Phys. Rev. B **65**, 214110 (2002).
[22] Y. Yao and J. S. Tse, Phys. Rev. B **75**, 134104 (2007).
[23] A. P. Jephcoat, H.-k. Mao, L. W. Finger, D. E. Cox, R. J. Hemley, and C.-s. Zha, Phys. Rev. Lett. **59**, 2670 (1987).
[24] H. Shimizu, T. K. N. Wada, S. Sasaki, Y. Yao, and J. S. Tse, Phys. Rev. B **77**, 052101 (2008).
[25] A. K. McMahan, Phys. Rev. B **33**, 5344 (1986).
[26] A. Dewaele, A.D. Rosa, N. Guignot, D. Andrault, J. E. Rodrigues, and G. Garbarino, Sci. Rep. **11**, 15192 (2021).
[27] F. Birch, J. Geophys. Res. **83**, 1257 (1978).
[28] A. Lazicki, P. Loubeyre, F. Occelli, R. J. Hemley, and M. Mezouar, Phys. Rev. B **85**, 054103 (2012).
[29] Y. Fei, A. Ricolleau, M. Frank, K. Mibe, G. Shen, and V. Prakapenka, Proc. Nat. Acad. Sci. USA **104**, 9182 (2007).
[30] A. Dewaele, F. Datchi, P. Loubeyre, and M. Mezouar, Phys. Rev. B **77**, 094106 (2008).
[31] R. J. Hemley, C. S. Zha, A. P. Jephcoat, H. K. Mao, L. W. Finger, and D. E. Cox, Phys. Rev. B **39**, 11820 (1989).
[32] P. Schwerdtfeger and A. Hermann, Phys. Rev. B **80**, 064106 (2009).
[33] T. Yagi, J. Phys. Chem. Solids **39**, 563 (1978).
[34] D. Walker, L. M. D. Cranswick, P. K. Verma, S. M. Clark, and S. Buhre, Am. Mineral **87**, 805 (2002).
[35] A. Dewaele, A. B. Belonoshko, G. Garbarino, F. Occelli, P. Bouvier, M. Hanfland, and M. Mezouar, Phys. Rev. B **85**, 214105 (2012).
[36] C. S. Barrett and L. Meyer, J. Chem. Phys. **41**, 1078 (1964).
[37] D. N. Batchelder, M. F. Collins, B. C. G. Haywood, and G. R. Sidey, J. Phys. C **3**, 249 (1970).
[38] H. Shimizu, H. Tashiro, T. Kume, and S. Sasaki, Phys. Rev. Lett. **86**, 4568 (2001).
[39] A. Dewaele, P. Loubeyre, F. Occelli, O. Marie, and M. Mezouar, Nat. Commun. **9**, 2913 (2018).
[40] B. Chen, A. E. Gleason, J. Y. Yan, K. J. Koski, S. Clark, and R. Jeanloz, Phys. Rev. B **81**, 144110 (2010).
[41] M. Ross, H. K. Mao, P. M. Bell, and J. A. Xu, J. Chem. Phys. **85**, 1028 (1986).
[42] P. Schwerdtfeger, R. Tonner, G. E. Moyano, and E. Pahl, Angew. Chem. Int. Ed. **55**, 12200 (2016).
[43] P. Schwerdtfeger, K. G. Steenbergen, and E. Pahl, Phys. Rev. B **95**, 214116 (2017).

[44] S. N. Vaidya and G. C. Kennedy, J. Phys. Chem. Solids **32**, 951 (1971).

[45] M. Ghafelehbashi, D. P. Dandekar, and A. L. Ruoff, J. Appl. Phys. **41**, 652 (1970).

[46] A. M. Pendas, J. M. Recio, E. Francisco, and V. Luana, Phys. Rev. B **56**, 3010 (1997).

[47] I. V. Aleksandrov, A. N. Zisman, and S. M. Stishov, Sov. Phys. JETP **65**, 371 (1987).

[48] A. Polian, J. M. Besson, M. Grimsditch, and W. A. Grosshans, Phys. Rev. B **39**, 1332 (1989).

[49] P. Schwerdtfeger, N. Gaston, R. P. Krawczyk, R. Tonner, and G. E. Moyano, Phys. Rev. B **73**, 064112 (2006).